Tunneling states of CN^- in various alkali halides: Study of resolved tunneling structures and "paraelastic sidebands" in the vibrational absorption of CN^-†

Hans U. Beyeler*
Department of Physics, University of Utah, Salt Lake City, Utah 84112
(Received 10 September 1974)

Tunneling structures were observed in the vibrational absorption of CN^- in KCl, KBr, KI, and RbCl using high-resolution ir spectroscopy. Under uniaxial stress applied in various directions two prominent effects were observed: (a) integrated absorption changes due to paraelastic alignment of the CN^- molecules and (b) drastic spectral changes due to the modification of the tunneling states under stress. In contrast to earlier work the structures could, in most cases, be fully resolved. In connection with (b), sidebands emerging from the vibrational absorption corresponding to transitions between different paraelastic states were observed, lending themselves to an accurate determination of paraelastic spittings. The results conclusively show that the equilibrium orientations of the molecule is along $\langle 111 \rangle$ axes in all investigated systems. Experimental evidence for a considerable stress dependence of certain tunneling matrix elements and deviations of the equilibrium orientations from $\langle 111 \rangle$ orientations under high stress lead to the introduction of a modified "soft" $\langle 111 \rangle$ tunneling model in which the effects of external stress on the defect-lattice interaction potential are not assumed to be negligible.

I. INTRODUCTION

Considerable effort has in recent years been concentrated on the study of orientational tunneling motion of defects in solids. In particular, a great amount of data has been accumulated on the three prominent systems Li^+, OH^-, and CN^- in KCl. Extensive references to these works are given in a review article on such phenomena by Narayanamurti and Pohl.[1] Although some of the results are still contradictory, others controversial, they have led to a basic understanding of tunneling systems to a point where further significant progress seems to depend largely on further improvements of the experimental techniques. A very promising breakthrough in this direction was recently achieved by Lüty[2] with the direct observation of a tunneling structure in the vibrational absorption of CN^- in KCl. It demonstrates that the powerful tool of high-resolution ir spectroscopy might eventually open a new dimension of insight into some tunneling systems.

Encouraged by Lüty's results, we set up an ir spectrometer with a maximal resolution power at 5 μm, the wavelength of the vibrational absorption of CN^-. Resolution superior to that of commonly used commerical instruments and adequate for the detailed study of a series of tunneling systems could be achieved with a conventional grating spectrometer without resorting to laser spectroscopy. This effort has proved to be extremely fruitful in that the tunneling structure of CN^- in KCl and its change under stress could be studied in full detail. In addition, "paraelastic sidebands," as discussed by Lüty,[2] could for the first time be observed and studied up to the highest achievable paraelastic splittings. The results reported here represent a great amount of new spectroscopic data on the CN^- systems studied. They fully confirm the $\langle 111 \rangle$ model proposed by Lüty from data taken under much more difficult experimental conditions and further supported by recent Kerr-effect measurements.[3] In the size of the observed tunneling splittings the results also agree with earlier comprehensive work[4,5] on CN^- systems; they differ, however, significantly and in the same way as those in Ref. 2 from the results in Refs. 4 and 5 as far as effects of elastic and electric fields are concerned and definitely rule out the formerly accepted $\langle 100 \rangle$ tunneling model.

The usual rigid $\langle 111 \rangle$ tunneling model (assuming a stress-independent defect-lattice interaction potential) was found to be a very useful first approximation for the interpretation of the data and is used extensively throughout this paper. There is, however, strong experimental evidence for a significant stress dependence of certain matrix elements and for stress-induced deviations of the molecular axes from exact $\langle 111 \rangle$ orientations. A modified "soft" tunneling model is thus introduced in which the defect-lattice interaction potential is significantly influenced by external perturbations. For the presentation of the rather complex data it will be helpful to have established first the relevant features of the $\langle 111 \rangle$ tunneling model.

II. RIGID $\langle 111 \rangle$ TUNNELING MODEL

Tunneling models have been treated in detail by Gomez *et al.*,[6] Shore,[7] Pfister,[8] and others. The

aspects of the ⟨111⟩ tunneling model relevant to this work have also been outlined in Ref. 2.

All results reported here have been obtained through the study of fine structures in the vibrational absorption; i.e., all observed transitions are combinations of a vibrational and a tunneling transition. We assume in the following the vibrational and tunneling motions to be independent. The tunneling level scheme is then identical for the first two vibrational states of importance here. Each direct transition between tunneling levels results then in two combined vibrational-tunneling transitions: a Stokes (vibrational and upward tunneling) transition and an anti-Stokes (vibrational and downward tunneling) transition. The frequencies of the two transitions are shifted to either side of the pure vibrational frequency by ΔU, the splitting between the two tunneling states involved. The matrix elements are identical for both components of a Stokes–anti-Stokes transition pair and are proportional to those of the direct tunneling transitions.

The intensities I_s and I_a of the two absorptions thus differ only by the population of the initial states according to

$$I_s/I_a = e^{\Delta U/kT}. \tag{1}$$

Equation (1) is completely independent of any specific tunneling model and constitutes a crucial test of the experimental results: If the observed structures are due to tunneling motion any observed Stokes–anti-Stokes absorption line pair has to obey Eq. (1). Since direct tunneling transitions are under the above assumptions readily translated into combined vibrational absorptions, we discuss for simplicity only the direct transition of a ⟨111⟩ tunneling defect. In the same spirit we shall later on interpret observed Stokes–anti-Stokes line pairs directly in terms of the participating tunneling transition.

The tunneling level scheme of a ⟨111⟩ defect with exclusively nearest-neighbor (nn) tunneling is given in Fig. 1 as a function of stress applied along ⟨111⟩ and ⟨110⟩ axes. For ⟨111⟩ stress the scheme is different from that given in Fig. 25 of Ref. 1, the latter being erroneous in some points. The tunneling wave functions for zero stress are, e.g., given in Ref. 6 and the matrix elements for electric dipole transitions between them can be derived straightforwardly. Solving the proper secular equations yields the wave functions and thus the transitions for any magnitude of stress splitting. The relevant selection rules and an example of this computation are given in the Appendix.

For practical reasons we divide the transitions into two groups: (a) All transitions under zero stress and those transitions under stress which occur between two levels of the *same* paraelastic multiplet we call the main tunneling transitions. The squares of the matrix elements (assuming a unit transition dipole along the axis of the defect) for the main transitions are indicated in Fig. 1. (Throughout this paper we designate with $E_\parallel$ and $E_\perp$ spectra or transitions for light polarized parallel and perpendicular to the applied stress, respectively. For ⟨110⟩ stress the three different polarizations are labeled with $E_\parallel^{\langle 110\rangle}$, $E_\perp^{\langle 1\bar{1}0\rangle}$, and $E_\perp^{\langle 001\rangle}$.) The values given for the transitions under

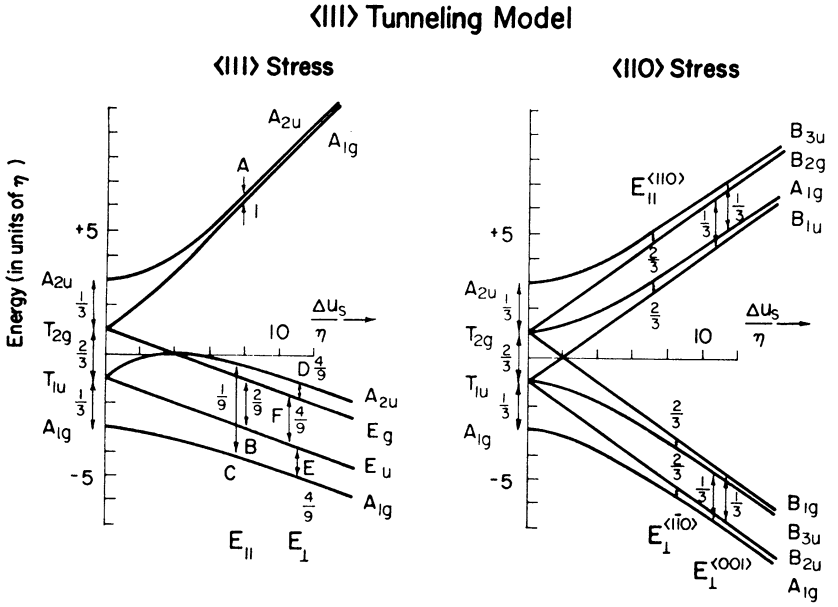

FIG. 1. Level scheme of a ⟨111⟩ dipole with exclusively nn tunneling as a function of an external stress applied along a ⟨111⟩ and a ⟨110⟩ axis. The energies are measured in units of the nn tunneling matrix element η. The horizontal axes are labeled with the elastic dipole splitting ΔU_s measured in units of η. The arrows indicate the electric dipole transitions for zero stress and in the high-stress limit.

stress in Fig. 1 are those for the limit stress splitting much greater than the tunneling splitting. The frequencies of all main transitions are at most of the order of the tunneling splittings; i.e., the main transitions cause a fine structure in a vibrational absorption with line splittings of the order of the tunneling splittings or less. (b) Additional transitions occur under stress between states of *different* paraelastic multiplets: Such transitions have (in contrast to the main transitions) no analog in a nontunneling system. These electric dipole transitions between paraelastic states are a hybrid between paraelectric and paraelastic resonance transitions; they may be compared to stess-tuned paraelectric transitions as studied by various authors [9-12] As such transitions are studied here in combination with a vibrational transition we shall call them *paraelastic sidebands* throughout this paper. For zero stress these transitions are part of the regular tunneling structure, but with increasing stress their frequencies continually increase (beyond those of the main transitions) according to the stress-induced paraelastic splitting ΔU_s (defined in the elastic dipole concept[13-16] by $\Delta U_s = \alpha S$, where S is the applied stress and α the paraelastic splitting factor).

The matrix elements of such transitions depend heavily on the elastic splitting ΔU_s and on the tunneling matrix elements. For high stress the matrix elements decrease as $(\Delta U_s)^{-1}$.

The tunneling transitions responsible for the paraelastic sidebands in the ⟨111⟩ tunneling model are indicated in Fig. 2. For some the matrix elements can easily be expressed in analytic form: e.g., under ⟨110⟩ stress the four transitions for $E_{\parallel}^{\langle 110\rangle}$ and $E_{\perp}^{\langle 1\bar{1}0\rangle}$ all have the same matrix element; its square is

$$\frac{16}{16+[\beta+(\beta^2+16)^{1/2}]^2}, \tag{2}$$

with $\beta = \Delta U_s/\eta$, where η is the nn tunneling matrix element. For ⟨110⟩ stress and $E_{\perp}^{\langle 001\rangle}$ there are no paraelastic sidebands within the assumptions of our model. The transitions indicated in Fig. 2 for $E_{\perp}^{\langle 001\rangle}$ occur only if other than nn tunneling is present and/or if the nn tunneling matrix element (under stress) differs in the two paraelastic states. In order to illustrate positions and intensities of the paraelastic sidebands these properties have been computed within the ⟨111⟩ tunneling model for a tunneling matrix element ($|\eta| = 0.63$ cm^{-1}) and an elastic dipole moment ($\alpha_{\langle 111\rangle} = 11.0\times10^{-24}$ cm^3) that correspond closely to the experimental situation for CN^- in KCl. In Fig. 3 the stress dependences of the sideband positions (top) are plotted together with the intensities of the Stokes transitions (bottom) as a function of the sideband splitting for $T = 2.5$ °K. The transitions are identified with the symbol for the polarization for which they occur and, if necessary, an additional index. Except for the transition $E_{\parallel}^2$ all sidebands emerge with increasing stress from the main tunneling absorption and for low stress their intensities are comparable to those of the main tunneling transitions.

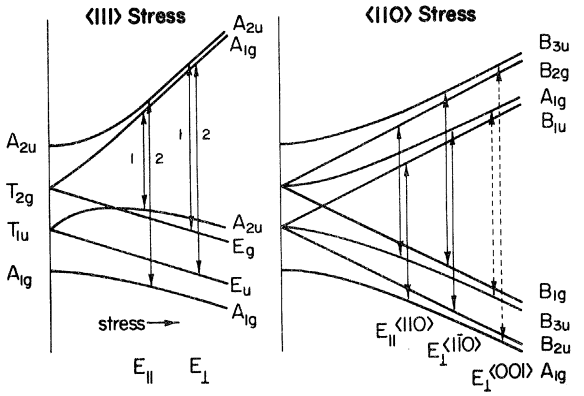

FIG. 2. Tunneling transitions between the stress-split states of a ⟨111⟩-oriented defect which give, in combination with a vibrational transition, rise to "paraelastic sidebands."

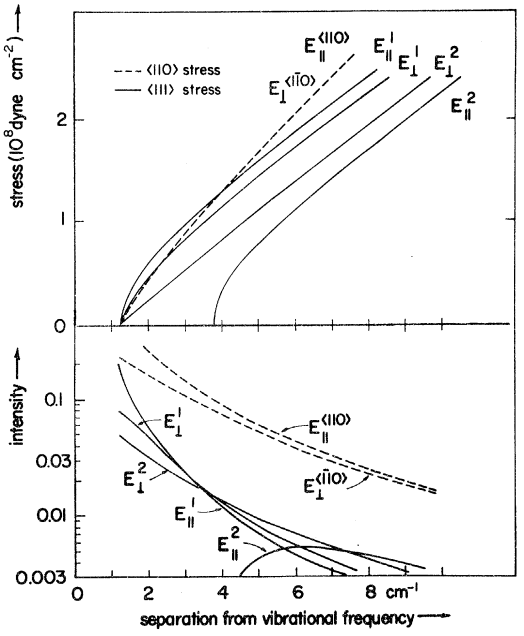

FIG. 3. Paraelastic sideband positions (top) and intensities (bottom) in the rigid ⟨111⟩ tunneling model with parameters that closely describe the experimental situation for CN^- in KCl.

III. EXPERIMENTAL TECHNIQUES

From the preceding outline two principal requirements for a successful experimental study of tunneling structures become evident: high resolution power for the investigation of the main tunneling transitions and high sensitivity for the detection of the weak paraelastic sidebands.

An ir spectrometer was therefore set up with highest achievable performance at 5 μm, in the region of the vibrational absorption of CN^-. The heart of the spectrometer was a Spex 1400 double grating monochromator operated in single-beam technique. The radiation was provided by a Nernst glower unit from Electro-Optical Industries, Santa Barbara, and detected with a photovoltaic, cooled InSb cell from Texas Instruments Co. with a peak detectivity D^* at 5 μm of 2.2×10^{11}. The 60 grooves/mm gratings were used in third order; the detection of other orders was suppressed by chopping the light with a highly CN^--doped KCl crystal, thus modulating the radiation within the sensitivity range of the detector in a narrow band at 5 μm only. The instrument was interfaced to a teletype; the spectra were analyzed and integrated on the departmental PdP-11 computer. In tests on water and $KCl:CNO^-$ absorption lines the instrument managed to resolve lines separated by 0.1 cm^{-1}. The radiation emerging from the monochromator was predominantly vertically polarized so that spectra for light polarized parallel to the vertically applied stress could be taken with a better signal-to-noise ratio than for light polarized perpendicular to the stress. The wire-grid polarizer provided nearly perfectly polarized light at 5 μm: Compare, e.g., the high-stress spectra in Fig. 4 which are completely different for both polarizations; none of the features of one spectrum is detectable on the other one.

For the study of the (rather broad) paraelastic sidebands the high resolution power of the instrument could be traded for high sensitivity to detect very weak absorption signals by opening the spectral slits of the monochromator. As background absorption and some residual superposition of different diffraction orders of the gratings could not completely be suppressed a stress-scan technique proved to be superior to the regular frequency-scan spectroscopy: The instrument was set at a fixed frequency above the vibrational absorption and the detector output recorded at regular intervals of the linearly increasing stress. The stress, smoothly increasing at an adjustable rate, was thereby produced by gradually pressurizing a bellows which in turn transmitted the force to a piston. With this technique paraelastic sidebands with a peak optical density of less than 0.01 cm^{-1} could be observed to pass by at a given frequency. The principal accuracy-limiting factor in this stress-scan spectroscopy is the smooth transmission of the pressure from the piston into the exchange-gas chamber of the cryostat and then onto the sample.

Extreme care had to be taken to produce very homogeneous stress. The stress dependence of the main tunneling structure (e.g., for ⟨100⟩ stress) and that of the paraelastic sidebands could directly be used to probe the stress pattern through the cross section of a sample with the focused beam of the instrument. The most homogeneous stress was achieved with the sample (about $4\times4\times12$ mm) between two stainless steel plates and a rigidly guided piston transmitting the force from the top of the cryostat via a steel ball to the plate on top of the crystal. Remaining minor inhomogeneities in the stress limit the accuracy of absolute values of determined elastic splittings to about ±15%.

In the stress experiments the sample was in thermal contact with the He bath through exchange gas.

The electric field experiments were performed

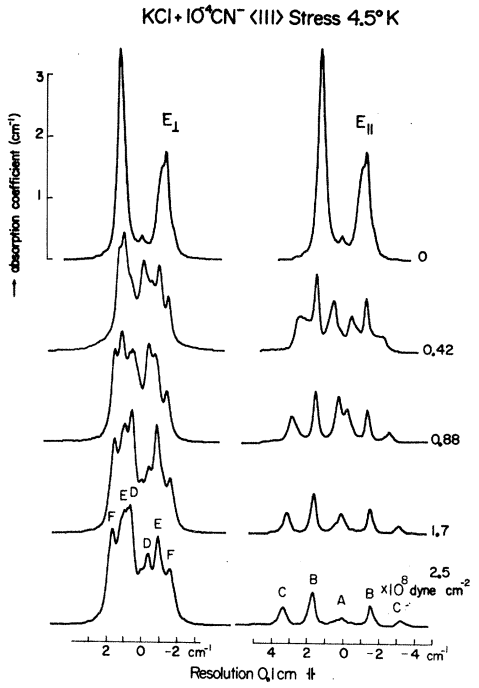

FIG. 4. Effects of ⟨111⟩ stress on the vibrational absorption of CN^- in KCl for light polarized perpendicular and parallel to the stress. The letters A–F identify Stokes–anti-Stokes line pairs in terms of the tunneling transitions in Fig. 1. (CN^- concentration expressed in the mole fraction of KCN content.)

with the same cryostat; to apply high electric fields at low temperatures the samples had to be immersed into superfluid helium. For these experiments the CaF_2 windows (glued with epoxy) at the experimental chamber were replaced by indium-sealed sapphire windows. Interferences in these windows resulted in a rather pronounced wavelength dependence of the transmitted light. Integrated absorptions could thus be determined with less accuracy in the electric field experiments than in the stress experiment where there was no such effect.

A crucial precondition for the successful study of tunneling structures was the availability of high-quality CN^--doped alkali-halide crystals from the departmental crystal-growth laboratory. Most experiments were performed on samples with a CN^- concentration of 10^{-4} (throughout this paper CN^- concentrations are given by the mole fraction of the KCN content of the sample). Samples from at least three different crystal-growth runs were studied for each host lattice as well as some samples with a higher CN^- content to ensure that all the structures under investigation here originate from isolated CN^- molecules. Special attention had to be focused on an absorption line appearing at low temperatures at the exact vibrational frequency. Although present in all investigated samples, the size of this line varied considerably among samples of the same host lattice and the same CN^- content. The possible origin of this line will be discussed later. For the study of the paraelastic sidebands higher CN^- concentrations, yielding higher optical densities of the sidebands, would have been desirable: Experiments on samples with a CN^- content of about 5×10^{-4}, however, showed that at this concentration the sidebands are already considerably broadened, possibly due to interaction between the CN^- centers, offsetting thus the advantage of a higher absorption.

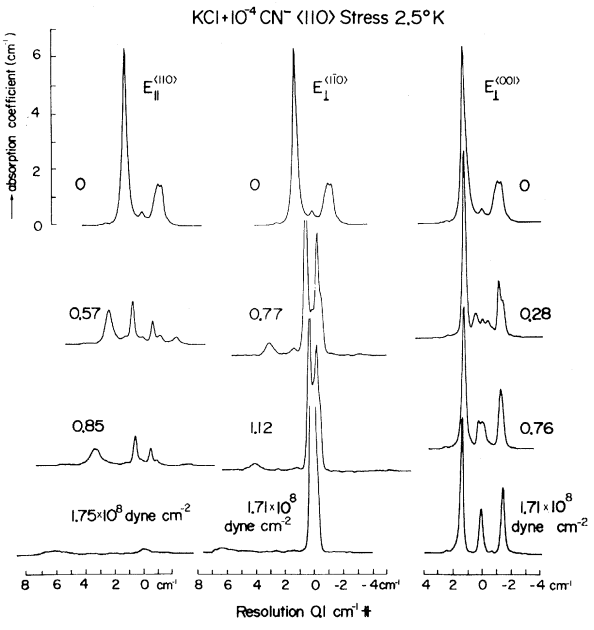

FIG. 5. Effects of ⟨110⟩ stress on the vibrational absorption of CN^- in KCl.

IV. EXPERIMENTAL RESULTS

The systematic study of the CN^- system in KCl, KBr, KI, and RbCl under ⟨100⟩, ⟨110⟩, and ⟨111⟩ stress with high resolution for the main tunneling structures as well as the stress-scan technique for the sidebands produced a large amount of new experimental material on these systems.

As all investigated systems were found to be basically similar, we limit the presentation of the results mainly to a detailed analysis of the model system CN^- in KCl, for which in accordance with earlier work the largest tunneling splitting was found.

A. CN^- in KCl

The zero-field tunneling structure and the effects of uniaxial stress on the vibrational absorption of CN^- in KCl are shown in Figs. 4–6. Only relative wave-number scales measuring splittings from the center are given. The absolute value of the vibrational frequency (2089 cm^{-1}) was found to agree within the limited absolute accuracy of the instrument with the value given by Seward and Narayanamurti.[4] None of the structures displayed is noticeably distorted by the instrumental resolution of 0.1 cm^{-1}. The zero-field double structure (we ignore here the small central peak, it will be discussed later in connection with the results in other host lattices) is consistent with the high-resolution spectrum given in Ref. 2.

Prior to interpreting the details of the observed structures the intensities of some of the fully resolved Stokes–anti-Stokes line pairs are checked for consistency with Eq. (1).

In Fig. 7 (left) $\ln(I_s/I_a)$ is plotted for CN^- in KCl against the reciprocal temperature. Within the restricted available temperature interval the experimental points are consistent with Eq. (1) with $\Delta U = 1.25$ cm^{-1}, the value derived from the spectra. Under ⟨100⟩ stress and $E_\parallel$ the splitting of the double structure was found to increase drastically. This effect permits us to test Eq. (1) as a function of ΔU without any further assumption on a specific tunneling model at this point. In Fig. 7 (right) $\ln(I_s/I_a)$ is plotted against ΔU with ΔU taken as one-half of the splitting between the two lines. The ex-

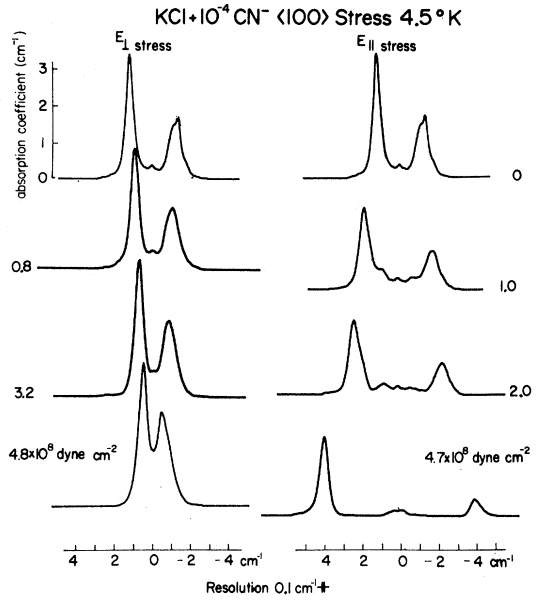

FIG. 6. Effects of ⟨100⟩ stress on the vibrational absorption of CN^- in KCl.

perimental intensities again obey Eq. (1) within experimental error.

In the further analysis we shall compare the results directly to the ⟨111⟩ tunneling model relying on the convincing evidence given by Lüty[2] and Gongora and Lüty[3] for ⟨111⟩-oriented ground states of CN^- in KCl. We shall, however, show how the validity of the ⟨111⟩ tunneling model for CN^- in KCl can also conclusively be deduced from the present results on ⟨111⟩ stress alone.

1. Analysis of zero-field structure

The zero-field absorption of a tunneling ⟨111⟩ dipole consists of three transitions (Fig. 1) which occur at the same frequency if other than nn tunneling is negligible. In this case the separation between Stokes–anti-Stokes vibrational absorptions is equal to four times the nn tunneling matrix element η, experimentally $|\eta| = 0.63\ \mathrm{cm}^{-1}$. Even a relatively small next-nearest-neighbor (nnn) tunneling matrix element μ would result in different frequencies for the three transitions. From the observed linewidth of 0.3 cm^{-1} of the two lines we can thus deduce an upper limit for μ: $|\mu| \leq 0.04\ \mathrm{cm}^{-1}$.

For clarity the rather complex stress effects are presented here in two steps: First we analyze the high-resolution vibrational spectra (connected to the main tunneling transitions) and thereafter we discuss the results of the stress-scan spectroscopy on the paraelastic sidebands. The original analysis had, of course, to include all stress effects on the vibrational absorption simultaneously.

2. Effects of ⟨111⟩ stress

Two principal stress-induced effects are evident in the high-resolution spectra in Fig. 4: (a) drastic spectral changes and (b) an increase in the total absorption for $E_\perp$ and a corresponding decrease for $E_\parallel$. In Fig. 8 the positions of the observed lines are compared to those derived from the ⟨111⟩ tunneling model with $\eta = -0.63\ \mathrm{cm}^{-1}$ and an elastic splitting factor $\alpha_{\langle 111\rangle} = 11 \times 10^{-24}\ \mathrm{cm}^3$ as determined later on from the paraelastic sidebands. The experimental results agree qualitative-

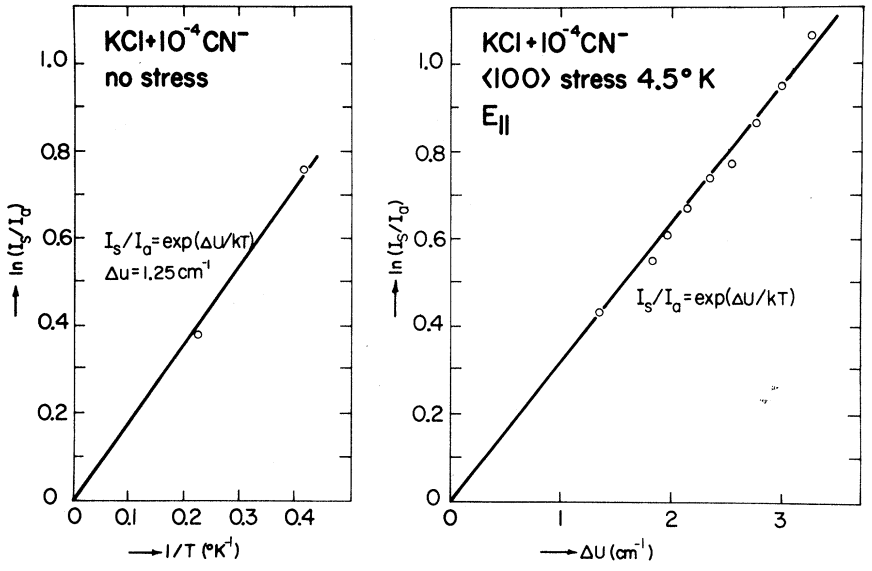

FIG. 7. Experimental intensity ratios of Stokes–anti-Stokes line pairs for CN^- in KCl; left: for zero stress and varying temperature; right: at constant temperature under ⟨100⟩ stress and $E_\parallel$ plotted as a function of the under stress increasing splitting ΔU of the lines from the center.

ly with the ⟨111⟩ tunneling model and the comparison in Fig. 8 permits the identification of the observed line pairs in terms of the involved tunneling transition as indicated by the letters A–F in Figs. 1 and 4. For ⟨111⟩ stress and $E_{\parallel}$ three tunneling transitions (A, B, C) are observed (not including the small initial center line). This fact positively excludes all other tunneling models, even the ⟨110⟩ model with predominant 90° tunneling which is in many respects similar to the ⟨111⟩ model (see discussion in Ref. 2). In that model only two transitions would occur in the situation considered here. In addition, both would occur within the upper paraelastic state resulting in a strong stress dependence of the line intensities, appreciably different from the behavior observed here.

The comparison in Fig. 8 evidences some systematic differences between model and experiment: for $E_{\parallel}$ in particular, instead of approaching asymptotically the stress-independent splittings at high stress given by the model the splittings continue to increase about linearly with stress. The most obvious explanation for this phenomena is that the stress enhances the tunneling motion in the lower paraelastic state so that the splitting between the four lower levels increases under stress. The five transitions observed between these levels permit an accurate determination of the tunneling matrix elements in this multiplet. The analysis shows that the matrix elements for other than nn tunneling remain negligibly small but that the nn tunneling increases appreciably under stress as shown in Fig. 9.

We shall further on call a system in which the tunneling parameters are considerably modified by an external stress a "soft" tunneling system in contrast to the "rigid" tunneling model outlined at the beginning of this paper where the tunneling matrix elements were assumed to be independent of the stress.

With the model confirmed by the analysis of the *positions* of the observed lines we may now check their *intensities* (which could be determined with less accuracy than the positions) for consistency with the model. In Fig. 10 the experimental total absorptions for $E_{\parallel}$ and $E_{\perp}$ are compared to those given by the ⟨111⟩ tunneling model. The same (constant) values for η and the paraelastic splitting factors are used here as in Fig. 8 (the effect of the increase in η on the stress-induced total-absorption changes is minimal).

For rather low stress the experimental points agree well with the model; for high stress the actual intensity for $E_{\parallel}$ is less than predicted by

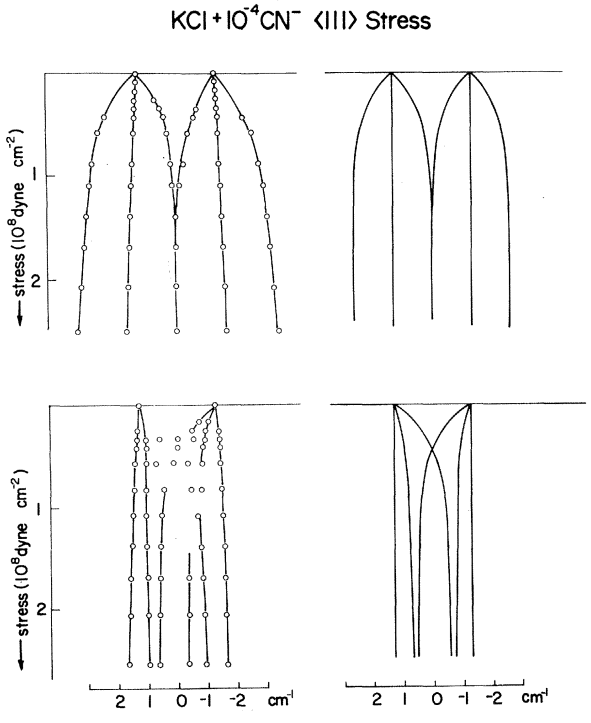

FIG. 8. Left: positions of the observed absorption lines under ⟨111⟩ stress; right: line positions according to the rigid ⟨111⟩ tunneling model, with the nn tunneling matrix equal to 0.63 cm^{-1} and an elastic dipole splitting factor $\alpha = 11.0 \times 10^{-24}$ cm^3.

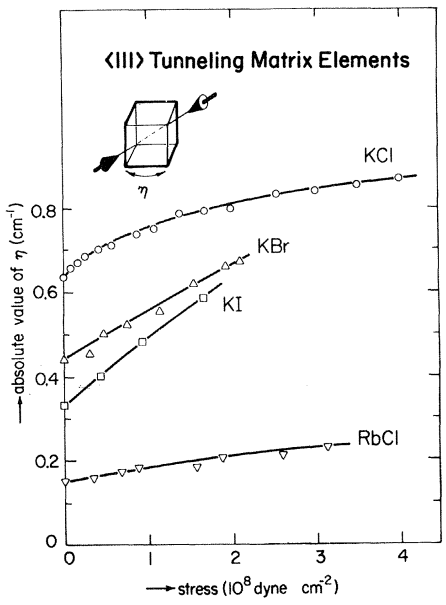

FIG. 9. Experimental nn tunneling matrix elements in the lower paraelastic state under ⟨111⟩ stress for CN^- in various host lattices.

the model and falls even below 25% of the initial value (which is for a ⟨111⟩ dipole the residual intensity for $E_\parallel$ at full alignment).

Although this discrepancy might be within experimental error, it more probably indicates another aspect of a soft tunneling system: The enhancement of the tunneling is likely to be accompanied by a deviation of the ⟨111⟩ wells which form the lower paraelastic state from ⟨111⟩ orientations towards orientations perpendicular to the stress axis. The larger decrease of intensity for $E_\parallel$ would then be accounted for by the decreasing component of the transition dipole along the stress axis. In the results on ⟨100⟩ stress stronger evidence for such effects to happen will be encountered.

For $E_\perp$ the optical density of the samples used reached under stress a value that made an accurate integration impossible. Also plotted in Fig. 10 is the intensity of line A alone which displays most drastically the paraelastic alignment. The agreement between model and experiment is fair; the experimental intensity is higher than the theoretical by an amount of the order of the intensity of the initial center peak.

No definite evidence of paraelastic sidebands can be found in the spectra in Fig. 4. Such sidebands were, however, easily detected on the high-energy side of the main vibrational absorption using the stress-scan technique. In Fig. 11 a series of such spectra is displayed for both polarizations with the spectrometer set at increasing distance from the main vibrational absorption. For $E_\parallel$ two clearly separate components are observed. The drastic baseline change observed in some of the spectra in Fig. 11 is due to the paraelastic intensity changes of librational sidebands situated at these frequencies. For $E_\perp$ two almost completely merged components were detected. The stresses at which the peaks of the sidebands were observed are plotted in Fig. 12 as a function of the splitting from the vibrational frequency. These experimental points are to be compared with the predictions from the rigid tunneling model in Fig. 3 The paraelastic splitting factor $\alpha_{\langle 111\rangle}$ would in principle have to be determined by fitting the experimental points in Fig. 12 to the ⟨111⟩ tunneling model using the experimental stress-dependent values for the tunneling matrix elements. But, as the points in Fig. 12 are appreciably scattered we simply deduce $\alpha_{\langle 111\rangle}$ from the range where the relation between sideband position and stress was found to be linear: $\alpha_{\langle 111\rangle} = 11.0 \times 10^{-24}$ cm^3. The experimental error of this value (±15%) is mainly due to residual inhomogeneities of the stress within the sample. The splitting factor $\alpha_{\langle 111\rangle}$ is related to the shape factor[15] $\lambda_1 - \lambda_2$ of the elastic dipole by

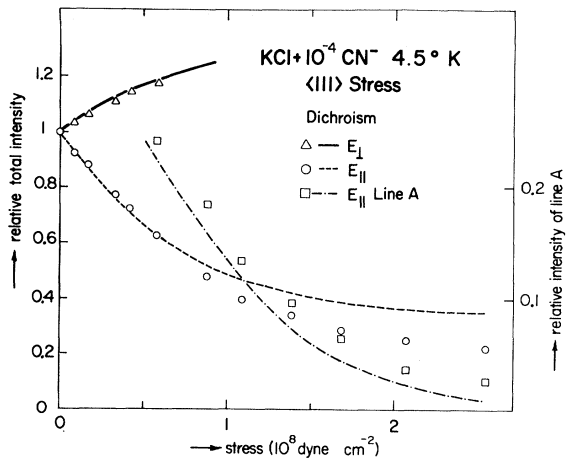

FIG. 10. Total intensity of the CN^- vibrational absorption in KCl under ⟨111⟩ stress for $E_\parallel$ and $E_\perp$ compared to those given by ⟨111⟩ tunneling model with the same parameters as in Fig. 7. Scale on right refers to the intensity of the line A alone ($E_\parallel$ spectrum).

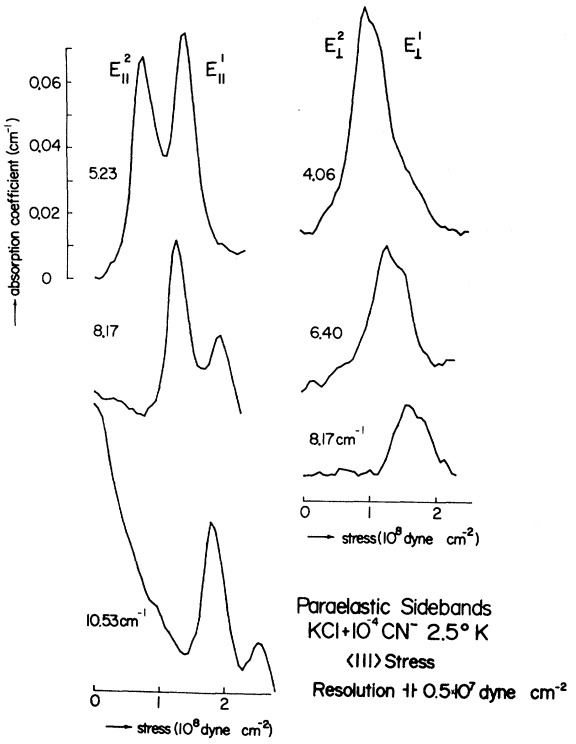

FIG. 11. Paraelastic sidebands as observed under ⟨111⟩ stress in the stress-scan technique. The parameter of the curves is the separation between the wavelength of the instrument and the center of the vibrational absorption.

$$\Delta U_s = \alpha_{\langle 111\rangle} S_{\langle 111\rangle} = \tfrac{8}{9} V_0(\lambda_1 - \lambda_2) S_{\langle 111\rangle}, \quad (3)$$

where V_0 is the volume of the primitive cell. Our value of $\alpha_{\langle 111\rangle}$ yields $\lambda_1 - \lambda_2 = 0.20$. This value is somewhat larger than that determined by Byer and Sack[17,18] from ultrasonic velocity measurements; they found $\lambda_1 - \lambda_2 = 0.156$. Lüty[2] deduced from stress-induced total-absorption changes of the vibrational absorption $\lambda_1 - \lambda_2 = 0.15$. The discrepancy between our present value and the earlier ones is appreciable, but it is probably within the sum of the errors of all parameters that enter into the experimental determination of elastic dipole moments.

Comparison of Figs. 1 and 2 makes evident that within the tunneling model the frequencies of the six main transitions (A–F) and the four sideband transitions are not all independent. The experimental results can thus be checked for internal consistency: At high stress, e.g., the horizontal separations in Fig. 12 of the two sidebands observed for each polarization, respectively, have to be identical to the splittings of the lines C (for $E_\parallel$) and B (for $E_\perp$) from the center in the spectra in Fig. 4. Within experimental error all the data were found to be fully consistent.

At very high stress considerable deviations from the linear elastic dipole behavior become evident (Fig. 12). These may indicate the breakdown of the elastic dipole concept for a soft tunneling system, but they may also be caused by an eventual coupling between paraelastic levels of the ground state and the librational state: At high stress the upper paraelastic state moves into the region of the librational levels. The nn tunneling mediates a coupling between levels of identical symmetry resulting in a nonlinear stress dependence of the energy levels wherever two levels of the same symmetry come close.

The analysis of the *intensities* of the paraelastic sidebands would in principle permit the determination of the (eventually stress dependent) tunneling matrix elements coupling the paraelastic states (e.g., between the $\langle 111\rangle$ and the $\langle 11\bar{1}\rangle$ wells). With the present stress-application mechanism the integrated line intensities were, however, found to scatter appreciably even within the same experiment, most probably due to a not completely smooth increase of the stress at the crystal; positions of the line maxima were considerably less affected by such perturbations. The general trend of a drastic decrease in intensity with increasing paraelastic splitting is evident from Fig. 12. Improvements of the experimental technique may in the future permit a more detailed analysis of sideband intensities.

One may finally come back to the question why the sidebands could not be observed in the direct spectra although their intensity is comparable to those of the main transitions for low stress. For $E_\parallel$ the drastic broadening of the main structure apparently makes an observation impossible until the sidebands are separated by several wave numbers from the center; at this point their intensity is already drastically reduced (see Fig. 3). For $E_\perp$ the sideband transitions contribute even for zero stress less than 20% to the total absorption. For a stress of 0.42×10^8 dyn cm^{-2} (second spectrum in Fig. 4) the sum of the two Stokes sidebands is reduced to 8% of the total absorption and for this stress the bands should just emerge from the feet of the vibrational structure. There are some indications of a broad line at the left (high energy) side of the main vibrational structure,

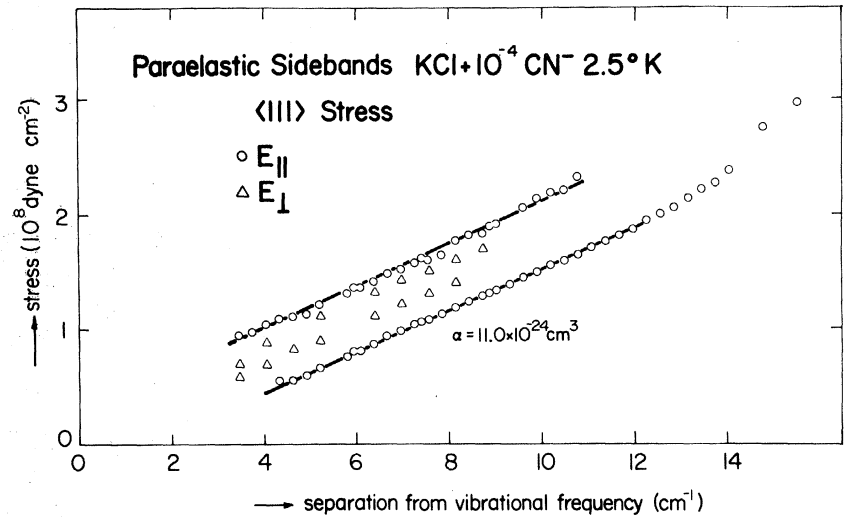

FIG. 12. Stress dependence of the sideband positions under $\langle 111\rangle$ stress. From the linear range a paraelastic splitting factor of 11×10^{-24} cm^3 is derived.

but there is certainly not enough evidence for a positive identification of a paraelastic sideband.

3. *Effects of ⟨110⟩ stress*

The spectral changes under ⟨110⟩ stress are illustrated in the high-resolution spectra in Fig. 5. For $E_{\parallel}^{\langle 110\rangle}$ and $E_{\perp}^{\langle 1\bar{1}0\rangle}$ the double structure narrows and at high stress becomes a single sharp line. Sidebands emerge at low stress from the structure, they move rapidly away from the center with increasing stress, and then they escape direct detection owing to their decreasing intensity. For $E_{\perp}^{\langle 001\rangle}$ a central line is formed at low stress but the double structure is retained to the highest applied stress. The total absorption decreases for $E_{\parallel}^{\langle 110\rangle}$, increases for $E_{\perp}^{\langle 1\bar{1}0\rangle}$, and remains about constant for $E_{\perp}^{\langle 001\rangle}$.

The spectral change of the absorption pattern according to the rigid ⟨111⟩ model can easily be derived from the transitions indicated in Fig. 1. The observed narrowing for $E_{\parallel}^{\langle 110\rangle}$ and $E_{\perp}^{\langle 1\bar{1}0\rangle}$ is fully consistent with the model. The single sharp lines at high stress indicate that the tunneling levels in fact pair up as given by the model. This in turn means that nnn tunneling is negligible even at high stress: A remaining separation between the levels merging at very high stress in Fig. 1 could only be explained by a nonvanishing nnn tunneling matrix element.

The sidebands emerging at low stress with an appreciable intensity are paraelastic sidebands directly observable here in the high-resolution spectra; they shall be discussed further in connection with the stress-scan spectra.

The interpretation of the $E_{\perp}^{\langle 001\rangle}$ spectrum is somewhat more complicated: The rigid tunneling model predicts no changes at all in the spectrum or in the integrated absorption. We interpret the absorption line pair moving at relatively low stress levels towards the center within the soft tunneling model as follows: The transitions involved in this line pair are assumed to be the two transitions for $E_{\perp}^{\langle 001\rangle}$ within the upper paraelastic states. The splitting between the two pairs of upper levels is given by the nn tunneling. This motion is drastically inhibited by the applied ⟨110⟩ stress because the nn tunneling motion in the upper paraelastic multiplet, e.g., from ⟨111⟩ to ⟨11$\bar{1}$⟩ leads through ⟨110⟩, i.e., through the elastically very unfavorable situation where the molecular axis is parallel to the stress axis. The nn tunneling in the lower paraelastic multiplet, on the other hand, e.g., from ⟨1$\bar{1}$1⟩ to ⟨1$\bar{1}\bar{1}$⟩, occurs in a plane perpendicular to the stress and is not much affected by the latter. The slight increase in the splitting of the two outer lines indicates in fact a small stress-induced increase of that motion. In view of the quite sizable stress-induced changes of tunneling matrix elements encountered for ⟨111⟩ stress and the even more drastic effects for ⟨100⟩ stress the above interpretation is not unrealistic. The only appreciable inconsistency concerns the intensity of the central line: Originating according to our interpretation in the upper paraelastic level it should reflect the same paraelastic intensity decrease as observed in the absorption for $E_{\parallel}^{\langle 110\rangle}$. Experimentally the intensity decreases only slightly with increasing stress and even after subtraction of the superposed small initial center peak the intensity is still inconsistent with the present interpretation. Two effects could account for that discrepancy: As evident from Fig. 5 strongly different spectral changes are observed for the two distinct polarizations perpendicular to the ⟨110⟩ stress. The samples have been carefully aligned for these experiments in order to avoid any cross talk between the two different spectra. In the specific case here the absorption in the other perpendicular polarization ($E_{\perp}^{\langle 1\bar{1}0\rangle}$) consists under high stress of an extremely narrow and strong central line; the divergence of the instrumental beam alone (total angle about 14°) may thus already cause the very strong $E_{\perp}^{\langle 1\bar{1}0\rangle}$ line to be noticeable even if the crystal is aligned for the $E_{\perp}^{\langle 001\rangle}$ geometry.

Part of the discrepancy may also be due to a deviation of the wells forcing the upper paraelastic states from the ⟨111⟩ orientations towards orientations perpendicular to the stress axis (e.g., from ⟨111⟩ towards ⟨001⟩) thus increasing the component of the transition dipole moment along ⟨001⟩.

From the model prediction in Fig. 3 it is evident that the paraelastic sidebands are more intense for ⟨110⟩ stress than for ⟨111⟩ stress; in addition, the two transitions each for the $E_{\parallel}^{\langle 110\rangle}$ and $E_{\perp}^{\langle 1\bar{1}0\rangle}$ geometry are according to the model completely superposed. These facts are reflected in the directly observed sidebands in Fig. 5 as well as in the superior signal-to-noise ratio in the stress-scan spectra in Fig. 13. The sidebands observed for $E_{\parallel}^{\langle 110\rangle}$ and $E_{\perp}^{\langle 1\bar{1}0\rangle}$ are quite sharp lines and there is no indication that they consist of two separate transitions. Within experimental error the sideband positions were identical in the $E_{\parallel}^{\langle 110\rangle}$ and the $E_{\perp}^{\langle 1\bar{1}0\rangle}$ polarizations. The experimental relationship between stress and sideband position is given in Fig. 14.

Since the lines could here be studied even for low stress where they emerge from the tunneling structure in the vibrational absorption the experimental points in Fig. 14 were analyzed by fitting them to the line positions derived from the ⟨111⟩ tunneling model with $|\eta| = 0.63\ \mathrm{cm}^{-1}$ and a best fitting paraelastic splitting factor $\alpha_{\langle 110\rangle}$. The

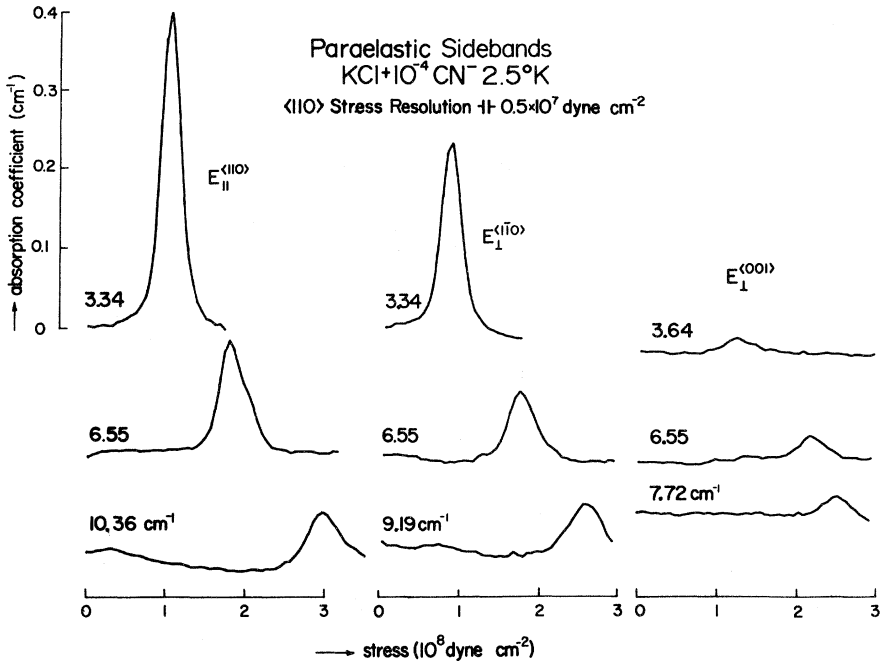

FIG. 13. Stress-scan spectra of paraelastic sidebands for stress applied along ⟨110⟩. The parameter of the spectra is the separation between the wavelength of the instrument and the center of the vibrational absorption.

solid line in Fig. 14 corresponds to $\alpha_{\langle 110\rangle} = 7.28 \times 10^{-24}$ cm^3 and fits the experimental points in a wide range.

The elastic dipole tensor of a ⟨111⟩-oriented defect has only one anisotropic component. Its splitting factors for ⟨111⟩ and ⟨110⟩ stress are related by

$$\alpha_{\langle 111\rangle}/\alpha_{\langle 110\rangle} = \tfrac{4}{3} . \tag{4}$$

We find here experimentally

$$\frac{\alpha_{\langle 111\rangle}}{\alpha_{\langle 110\rangle}} = \frac{11.0\times10^{-24}\ \text{cm}^3}{7.28\times10^{-24}\ \text{cm}^3} = 1.51 . \tag{5}$$

This experimental value is independent of the calibration of the applied stresses and is therefore more accurate than the stress-splitting factors themselves. Complementary experiments with ⟨111⟩ and ⟨110⟩ stress yielded ratios very close to that in (5) so that the discrepancy between (4) and (5) is probably genuine. It may reveal yet another aspect of a soft tunneling system. It should be pointed out here that the elastic dipole concept[13-16] rests on the assumption that the stress fields produced by the misfitting impurity in the surrounding host lattice are large compared to any externally produced stress. In a system like CN^- in KCl this assumption may not be valid.

The shape factor $\lambda_1 - \lambda_2$ computed from $\alpha_{\langle 110\rangle}$ is 0.176, closer to the values given by Byer and Sack[17,18] (0.156) and Lüty[2] (0.15), than the one derived earlier in this work from $\alpha_{\langle 111\rangle}$ (0.20).

At high stress deviations from linearity (and thus from the rigid-tunneling-model behavior) are noticeable; the situation is similar to that under ⟨111⟩ stress and the comments made there apply to the ⟨110⟩ stress results as well.

A separate analysis is required for the $E_\perp^{\langle 001\rangle}$ spectra: Only very weak sidebands are observed for this polarization, the lines were detected only above a certain splitting from the vibrational frequency, and the dependence of the line intensities on the stress is completely different from that observed in the other polarizations. In the rigid ⟨111⟩ tunneling model paraelastic sideband transitions occur for $E_\perp^{\langle 001\rangle}$ only if other than nn matrix

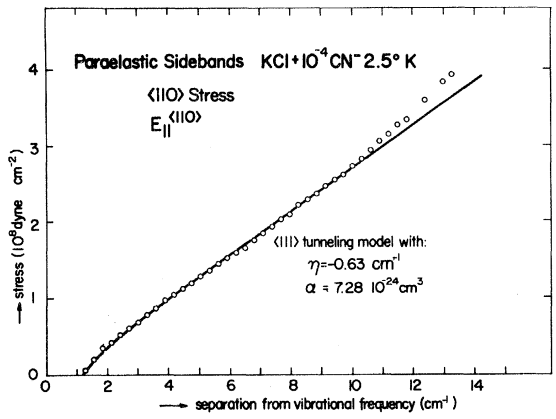

FIG. 14. Stress dependence of the position of the paraelastic sideband under ⟨110⟩ stress.

elements are nonzero. In the soft tunneling model they occur in addition if the nn tunneling matrix elements for both paraelastic states differ under stress. If the observed lines were due to a small, but nonvanishing and stress-independent nnn tunneling motion the line intensity would have to vary with stress in the same way as the lines observed for the other polarizations. The actual intensities (increasing slightly with stress, see Fig. 13) rather suggest that stress-induced changes in the tunneling matrix elements are responsible for the observed effects. The present results are therefore further support for the interpretation of the high-resolution $E_\perp^{\langle 001\rangle}$ spectrum given earlier.

4. *Effects of ⟨100⟩ stress*

Quite noticeable spectral changes were observed under ⟨100⟩ stress (see Fig. 6): the double structure is preserved in both polarizations, but for $E_\parallel$ the splitting increases with the stress and reaches 8 cm^{-1} for the highest achieved stress; for $E_\perp$ the splitting decreases sizeably. Such effects are already mentioned in Ref. 2. The spectral changes are accompanied by a moderate increase of the integrated absorption for $E_\perp$ and a corresponding decrease for $E_\parallel$ as shown in Fig. 15.

Within the rigid ⟨111⟩ model no changes at all are expected under ⟨100⟩ stress. The reasons for the observed effects have therefore to be found in the softness of the defect-lattice interaction potential. The ⟨100⟩ stress reduces the symmetry of the lattice site to tetragonal and nn tunneling motions parallel and perpendicular to the stress axis (η' and η in Fig. 16) need not remain equal. For $E_\parallel$ the tunneling parallel to the stress determines the observed splitting: This motion is apparently enhanced by the stress. For $E_\perp$ one "looks at" the tunneling perpendicular to the stress; this motion appears to be inhibited by the stress.

The stress dependence of the tunneling matrix elements derived from the structural changes are displayed in Fig. 16.

The simultaneous changes in the integrated absorption indicate that the changes in the tunneling motion are related to deviations of the equilibrium orientations of the defect from ⟨111⟩ axes towards orientations perpendicular to the stress; e.g. (assuming stress applied along ⟨001⟩), the ⟨111⟩ and the ⟨11$\bar{1}$⟩ minimum wells of the defect lattice interaction are moved towards ⟨110⟩, resulting in an enhanced tunneling motion (η') between the two wells and a reduced component of the transition dipole moment parallel to the stress. On the right axis in Fig. 15 the angular deviation ($\Delta\phi$) from ⟨111⟩ towards ⟨110⟩ that produces the corresponding change in the integrated absorption is given.

Using the stress-scan technique a search for paraelastic sidebands under ⟨100⟩ stress was conducted in various samples. With the highest instrumental sensitivity no indications at all could be found for the existence of such sidebands under ⟨100⟩ stress. This negative result is in full agreement with the ⟨111⟩ tunneling model and also in accordance with the above interpretation of the

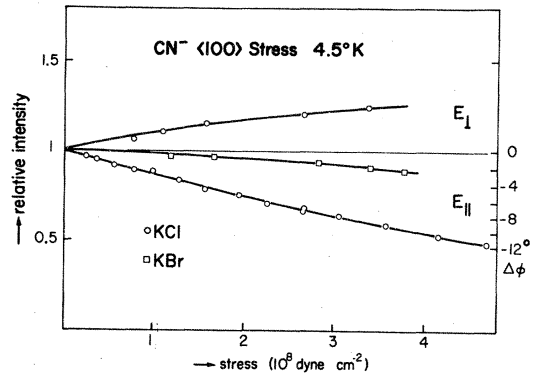

FIG. 15. Changes in the integral of the CN^- vibrational absorption under ⟨100⟩ stress in KCl and KBr. The observed effects are attributed to a rotation of the vibrational transition dipole moment by $\Delta\phi$ from ⟨111⟩ orientations towards a plane perpendicular to the stress. For ⟨001⟩ stress, e.g., the ⟨111⟩ and ⟨11$\bar{1}$⟩-oriented dipoles are rotated by $\Delta\phi$ [in the (1$\bar{1}$0) plane] towards to the ⟨110⟩ direction.

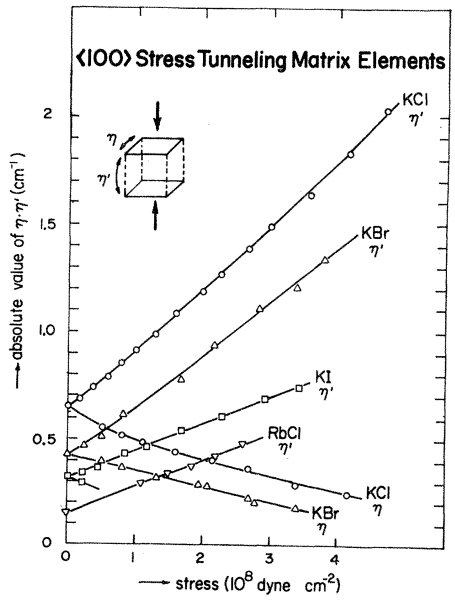

FIG. 16. Experimental nn tunneling matrix elements for CN^- under ⟨100⟩ stress for various host lattices.

⟨100⟩ stress effects: As discussed in detail in Ref. 2, the second moment of the *total* vibrational absorption (in the high-temperature limit and neglecting all line-broadening mechanisms) is a direct measure for the tunneling motion is a system. The narrowing of the main vibrational absorption under stress (as, e.g., for a ⟨111⟩ defect under ⟨110⟩ stress and $E_{\perp}^{\langle 110\rangle}$ polarization) is therefore (in a system with *constant* tunneling matrix elements) always accompanied by emerging paraelastic sidebands which compensate for the decreasing second moment of the central structure. If the observed ⟨100⟩ stress effects were due to a paraelastic alignment rather than a change in the tunneling parameters, then sidebands should be present for $E_{\perp}$ to compensate for the narrowing of the central structure.

5. *Effects of electric fields*

The effects of electric fields on the vibrational absorption have been studied by Pompi and Narayanamurti.[5] They found a slight decrease of the total absorption for light polarized parallel to the field applied along a ⟨100⟩ axis. Their results could not be explained in any simple model of a reorienting dipole and unrealistic lattice distortions were held responsible for the observed effects.

In view of the present more detailed understanding of the CN^- systems, the electric field effects have been reinvestigated. Our results are illustrated in Fig. 17 for a ⟨100⟩ electric field and light polarized parallel to the field.

In this geometry we observed a field-induced rather narrow central peak and a slight outward movement of the two main tunneling lines; the total absorption remained unchanged within the experimental error of ±10%. In a series of measurements with different samples and fields applied in various directions no significant change in the integrated absorption could be detected in any situation and none of the results reported in Ref. 5 could be reproduced.

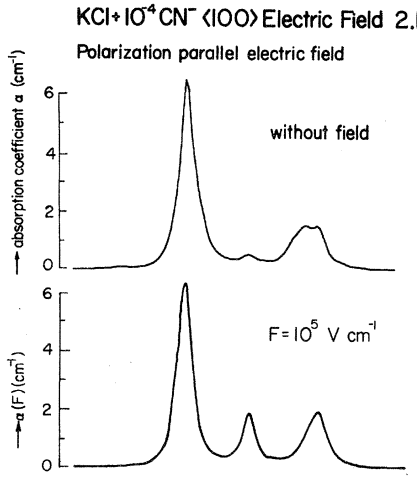

FIG. 17. Effects of a ⟨100⟩ electric field of 10^5 V cm^{-1} on the vibrational absorption of CN^- in KCl at 2.1 °K.

The level scheme of a ⟨111⟩ defect in an electric field is, e.g., given in Ref. 6. For a field applied in any direction there are always two principal structural changes in the vibrational absorption spectrum for light polarized parallel to the field: (a) a growing absorption at the pure vibrational frequency due to direct dipolar transitions as the electric field restores dipolar states from the nondipolar tunneling states; and (b) an outward movement of the initial tunneling lines (again the second moment of the complete absorption remains constant as long as the tunneling parameters are unchanged, see Ref. 2). With increasing electric field the tunneling transitions become paraelectric resonance transitions, their frequency continually increases as the tunneling states are gradually split into the various paraelectric states. In the vibrational absorption the tunneling lines move outwards and become "paraelectric sidebands." The electric field effect on the high-resolution spectrum in Fig. 17 is completely consistent with that expected from the ⟨111⟩ tunneling model; however, even the highest achieved electric field induces only a small modification of the tunneling states and only the beginning of the expected spectral change can be studied. Measurements with fields applied in other directions and also with light polarized perpendicular to the field yielded similarly model-consistent results.

From a quantitative comparison between model and experiment the electric dipole moment p of the defect can be determined. But, as the spectral changes for low fields are quadratic in the electric field, no accurate value for p could be deduced here from the rather small observed effects. We get $p = 0.4 \pm 0.1$ D consistent with the value of 0.3 D determined by Sack *et al.*[19,20] from dielectric measurements. The total absorption of a ⟨111⟩ defect in a ⟨100⟩ electric field remains strictly constant in both polarizations. For ⟨111⟩ and ⟨110⟩ electric fields one expects changes in the integrated absorption of at best 4% assuming $p = 0.4$ D, a maximal electric field of 1.2×10^5 V cm^{-1} and $T = 2.1$ °K. Experimentally no significant change of the total absorption could be observed for any situation, but due to interference effects in the sapphire windows the accuracy of the determined integrated absorptions is not better than ±10%.

B. CN^- in KBr, KI

The zero-field tunneling structures of CN^- in KBr and KI are compared in Fig. 18 to that of KCl. With increasing lattice parameter the absorption appears to shift gradually from the two satellites into a central line. The relative intensities of the central line and the satellites were again found to vary appreciably among samples of the same host lattice. Despite this quite remarkable difference in the zero-field structures the effects of uniaxial stress were found to be very similar to those in KCl both in the structural changes and the change of the integrated absorptions. The symmetrical satellites in the zero-field structures thereby play the role of the two principal lines in KCl. The center line remained superposed on the tunneling structure with no noticeable change in linewidth or intensity; it did in no case participate in the structural changes; i.e., no Stokes–anti-Stokes line pairs were observed to emerge from the center line.

In many situations a complete analysis of the structural changes was not possible because some components were "buried" in the center line. For $\langle 111 \rangle$ stress and $E_{\|}$ the structures could, however, be observed in full detail and based on the arguments given in the interpretation of the corresponding KCl spectrum one can again conclusively deduce the validity of the $\langle 111 \rangle$ tunneling model for CN^- in KBr and KI.

From the satellites in the zero-field structures we deduce the nn tunneling matrix element: $|\eta| = 0.43\ cm^{-1}$ for KBr and $0.33\ cm^{-1}$ for KI. Under $\langle 111 \rangle$ and $\langle 110 \rangle$ stress manifestations of the softness of the defect-lattice interaction could again be observed; the stress-induced changes in the matrix elements (Figs. 9 and 16) are almost as dramatic as for CN^- in KCl. In KBr a small change in the total absorption was again observed under $\langle 100 \rangle$ stress (Fig. 15). For $\langle 110 \rangle$ stress and $E_{\perp}^{\langle 001 \rangle}$ the spectrum is in both KBr and KI similar to that in KCl and the interpretation given there applies most probably to these two systems, too.

Paraelastic sidebands have been detected for $\langle 111 \rangle$ stress and $\langle 110 \rangle$ stress both in KBr and KI, whereas for $\langle 100 \rangle$ stress no indication of sidebands was found. For $\langle 111 \rangle$ stress the sidebands were quite weak and could not be followed further out than 5–6 cm^{-1} from the vibrational frequency. The two transitions occurring at slightly different stresses were in all cases merged into a broad line which made even an approximate determination of the paraelastic splitting factor impossible. Under $\langle 110 \rangle$ stress the sidebands were still strong enough to be observed up to the highest achieved stresses. For $E_{\|}^{\langle 110 \rangle}$ and for $E_{\perp}^{\langle \bar{1}10 \rangle}$ the sidebands were again found to be at identical positions. In Fig. 19 the stress-dependent sideband positions are given for this situation for CN^- in KBr and KI; best fits to the tunneling models yield the following elastic splitting factors:

$9.7 \times 10^{-24}\ cm^3$, for KBr;

$15.7 \times 10^{-24}\ cm^3$, for KI .

The corresponding shape factors $\lambda_1 - \lambda_2$ are

0.20, for KBr,

0.27, for KI.

Byer and Sack[17,18] determined from ultrasonic attenuation measurements: $\lambda_1 - \lambda_2 = 0.198$ for KBr and 0.162 for KI. A series of measurements con-

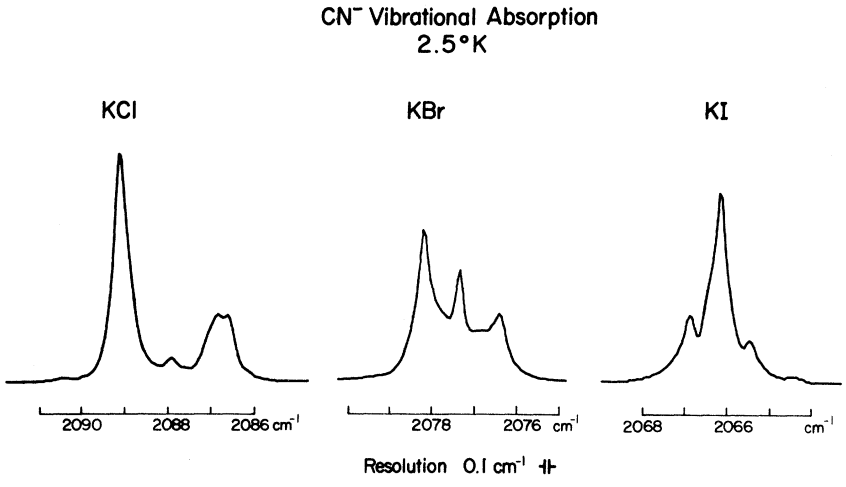

FIG. 18. High-resolution CN^- vibrational absorption spectra in KCl, KBr, and KI at 2.5 °K.

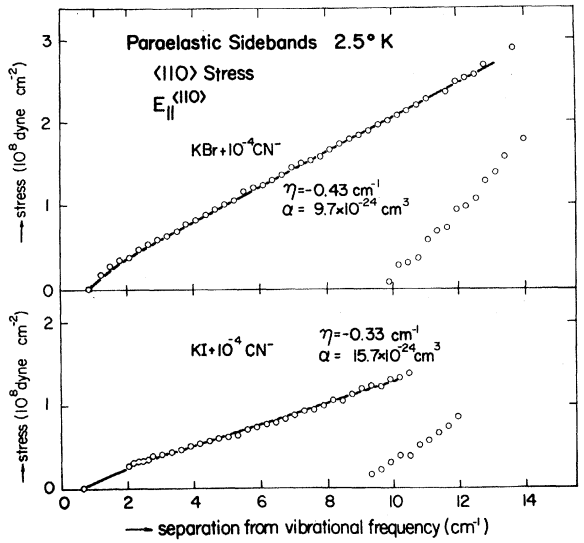

FIG. 19. Positions of the paraelastic sideband under ⟨110⟩ stress for KBr and KI.

firmed our values quoted above and we have no explanation for the considerable discrepancy in the values for KI.

In contrast to KCl rather strong sidebands emerging from librational absorptions could be observed here for ⟨110⟩ stress. Their stress dependence corresponds to a paraelastic splitting factor appreciably lower than the one for the ground state.

For $E_{\perp}^{\langle 001\rangle}$ extremely weak sidebands were observed in a very restricted range of splittings.

C. CN^- in RbCl

The zero-field vibrational absorption of CN^- in RbCl consists of a structureless broad line. Experiments with ⟨100⟩ and ⟨111⟩ stress showed, however, that this system is merely a step further in the tendency observed from KCl to KI in Fig. 18. Without stress a tunneling structure is hidden within the broad structure, and whenever in the other host lattices the tunneling structure has become larger under stress, lines were observed to emerge from the broad central absorption in RbCl. The results strongly suggest that the equilibrium orientations are in this system along the ⟨111⟩ axes too; but the system has not been fully analyzed as the tunneling structures are only partially observable due to the dominant center line. For ⟨111⟩ and ⟨100⟩ stress the change of the matrix elements under stress could be determined and is displayed in Figs. 3 and 16. Paraelastic sidebands were again observed for ⟨111⟩ and ⟨110⟩ stress.

V. INTERNAL ELASTIC AND ELECTRIC FIELDS—THE ORIGIN OF THE CENTRAL LINE

The "good" agreement between the CN^- system studied and the ⟨111⟩ tunneling model holds only if the central line in the spectra is not considered to be a part of the regular tunneling structure, i.e., if a separate group of nontunneling CN^- molecules is held responsible for that central line. Various observations support this assumption: (a) The intensity of the central line is not strictly related to that of the outer lines but varies among samples of the same host lattice, same CN^- concentration, but different crystal-growth runs (see Fig. 20); (b) in a crystal with deliberate OH^- doping the central line was exceptionally high; (c) for no investigated stress the line was found to participate in the structural changes—if it were a transition between two accidentally degenerate tunneling levels one would expect these levels to be split under a certain stress, so that the central line would break up into a Stokes–anti-Stokes line pair; (d) the line was found to be greatly increased after a sample had been stressed beyond its elas-

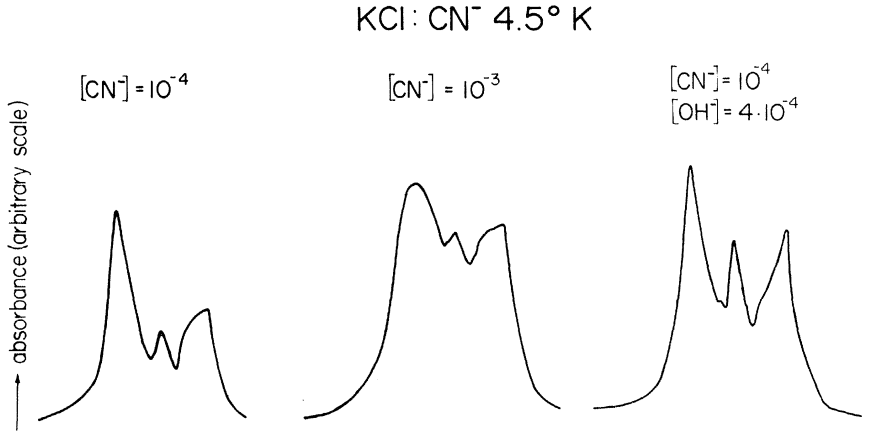

FIG. 20. High-resolution spectra of three different CN^--doped KCl crystals.

tic limit; and (e) the central line is unproportionally strong in samples with a higher CN^- concentration (Fig. 20). It appears realistic to assume that a certain number of CN^- molecules is always locked in its tunneling motion by the interaction with other defects, internal strain, or other crystal imperfections.

The presence of internal elastic and electric fields of considerable strength in alkali halides has been deduced from various experiments.[9,21-25] We shall therefore briefly review the possible effects of internal fields on the high-resolution spectra discussed in this paper.

The effects of random internal stress are difficult to evaluate directly from the presented spectra for uniaxial stress applied in special symmetry directions; in these situations several of the eight ⟨111⟩ orientations remain always degenerate leading to tunneling-split paraelastic multiplets; a tunneling splitting in the main absorption is thus is many cases retained under stress. Under random stress, on the other hand, the degeneracy between the eight wells is likely to be lifted completely (except for the wells connected by 180° tunneling, which remain degenerate as long as the stress is homogeneous within the region of the defect). The infrared spectrum consist then of pure vibrational transitions (plus unobservable, broad paraelastic sidebands). The elastic energy required for such a localization is of the order of the tunneling splitting, i.e., about 1 cm^{-1} in KCl. This corresponds to a stress of about 2×10^7 dyn cm^{-2}. In a more detailed analysis one would have to compute the level scheme and transitions of the defect for any stress and randomize the spectrum properly. But the above estimate suggests strongly that internal stresses of the order of $(6-8) \times 10^7$ dyn cm^{-2}, as they have been derived from other experiments on defects in alkali halides, would already result in a much larger central peak than actually observed in KCl.

At higher CN^- concentrations elastic dipole-dipole interaction may be responsible for the increase in the center peak. Muggli[14] has computed the elastic interaction between elastic dipoles within continuum elasticity theory and his theoretical results have been confirmed by an experimental investigation of the interaction between O_2^- centers.[26] Applying these results to two CN^- molecules at the average statistical distance for a concentration of 10^{-3} leads to an interaction energy of the order of about 3 cm^{-1}, enough to alter the vibrational absorption structure appreciably. This may explain the increased central peak (Fig. 20) observed in the sample with a CN^- concentration of 10^{-3}.

An upper limit to the magnitude of internal stresses is also given by the linewidth of the observed paraelastic resonance lines, which is in KCl about 2.8×10^7 dyn cm^{-2} (for ⟨110⟩ stress). The lines were found to be considerably smaller at 2.5 than at 4.5 °K. Part of the linewidth may thus even at 2.5°K be due to the interaction with phonons; a further contribution may come from stress inhomogeneities, so that the actual level of internal stresses is probably considerably lower than 2.8×10^7 dyn cm^{-2}.

The effects of internal electric fields are easier to evaluate. For the polarization parallel to the field there is always a sharply increased central line due to the dipole states restored by the electric field from the tunneling states. In a random distribution this effect leads directly to an isotropic increase of the central line. Owing to the small electric dipole moments large random fields of about 10^5 V cm^{-1} would be required to account for the central line in KBr or KI. In the crystal doped with both CN^- and OH^- (Fig. 20), on the other hand, the interaction with the large electric dipole moment of the OH^- ion may well account for the observed increase in the central peak.

In conclusion it is thus likely that the central peaks in the low-concentration samples are caused by CN^- molecules perturbed principally by internal strain fields; those often-cited internal fields were, however, at least in the KCl samples used here, considerably smaller than commonly assumed.

Comparing the structures in the various host lattices one has then to account for the drastic increase in the central peak from KCl to KI whereby the tunneling splitting is only reduced by a factor of 2. Even taking into account the larger elastic dipole moment in KI it is not possible to explain the increase in the center line if one assumes the internal fields to be of the same magnitude in both KCl and KI. The systems with smaller tunneling splittings appear to be systematically more susceptible to perturbations impeding the observation of a tunneling structure (in RbCl) even when the "unobscured" tunneling splitting would still be within the resolution of the instrument. One might further add to this list OH^- in KCl, where clear evidence for tunneling motion was found[27-29] corresponding to a level splitting in the ground state of about 0.3 cm^{-1}, but where no structure at all can be detected under any circumstances in the vibrational absorption.[30]

VI. RIGID ASPECTS OF THE CN^- SYSTEMS

In the analysis of the data we have often emphasized the "soft" aspects of the CN^- systems studied as this feature could for the first time be studied

in detail. It should nevertheless be kept in mind that in the systems investigated the CN^- molecules are (at least at He temperature) strongly localized in the ⟨111⟩ minimum wells by a considerably anisotropic defect-lattice interaction. The tunneling motion is completely restricted to the nn paths ("along the edges of a cube"). The tunneling splitting of 1.25 cm^{-1} between the ground-state levels is still small compared to the librational energy (about 11.5 cm^{-1}) so that a tunneling model based only on localized librational ground states still adequately describes the systems. At least for moderate stress the induced paraelastic splitting is linear and the molecules remain essentially oriented along ⟨111⟩ axes; the externally produced elastic fields thus do not entirely modify the local defect structure. In particular, all observed softness effects are of gradual nature and no "phase transition" (as, e.g., the change of the equilibrium orientations from ⟨111⟩ to ⟨100⟩ or ⟨110⟩) occurs.

We did not present here any high-resolution results on the librational sideband situated 11 cm^{-1} above the vibrational structure[2,4] as no new features could be resolved in this rather broad absorption. It is, however, noteworthy here that the position of this sideband was not found to be noticeably influenced by any type of applied stress. It thus appears that even the curvature of the minimum wells is not very sensitive to externally produced elastic fields.

VII. "SOFT" ASPECTS OF THE CN^- SYSTEMS

The two prominent manifestations of the softness of the defect-lattice interaction are (a) appreciable changes in the tunneling matrix elements and (b) deviations of the equilibrium orientations from the ⟨111⟩ axes under stress.

Despite the large amount of available experimental data on reorienting crystal defects (e.g., on their equilibrium orientations, reorientational barrier, and elastic dipole moment) there is at present no comprehensive theory relating the observed properties to microscopic parameters. In this experimental paper we thus limit ourselves to some considerations on the relative size of the two softness effects.

Tunneling motion through a barrier depends strongly on both the width and the length of the barrier. In our results changes in the barrier widths are directly measured by the angular deviations of the molecular axes from ⟨111⟩ orientations. We may then ask whether the observed changes in the barrier *widths* alone may already account for the stress dependence of the tunneling matrix elements assuming the barrier *heights* to remain constant. No analytic expression is known relating the tunneling probability to barrier parameters in a two-dimensional potential. The tunneling motion η' in Fig. 16 which greatly increases under ⟨100⟩ stress may, however, be regarded as essentially one dimensional at least for high stresses where the other tunneling motions are (in KCl) more than 7 times smaller. We can then use the one-dimensional expression derived in many textbooks on quantum mechanics for the tunneling matrix element η across a barrier $V(\theta)$[31]:

$$\eta = \left(\frac{E}{\pi}\right) \exp\left[- \int_{-\theta_1}^{+\theta_1} \left| \left(\frac{1}{B}[V(\theta) - E)\right)^{1/2} \right| d\theta \right], \tag{6}$$

where E is the particle energy (librational ground-state energy), B the rotational constant, and $\pm\theta_1$ the angles for which $V(\pm\theta_1) = E$.

We approximate the barrier for the η' tunneling motion under ⟨001⟩ stress by a rectangular barrier of width a and height V_0. We assume the width a to be 35°, i.e., half the complete tunneling path of 70.5° from ⟨111⟩ to ⟨11$\bar{1}$⟩. For the other parameters we use the values of the best-fitting hindered rotator ($K^4 = -9.6$, $K^6 = -11.6$) as discussed later on in this paper, where from the potential and the level scheme follows: $V_0 = 43.5$ cm^{-1}, $E = 24.5$ cm^{-1}, $B \sim 1$ cm^{-1}. With these values we obtain $\eta = 0.54$ cm^{-1}. Considering all the simplifications the agreement with the actual zero-stress value of 0.63 cm^{-1} is strikingly good; but this is in fact merely a test for the validity of the simplifying assumptions, as we have only duplicated the hindered-rotator model calculation for the "best-fit" potential (which can be regarded as a complex model yielding the tunneling matrix elements for a two-dimensional potential) with the one-dimensional expression (6). For a ⟨100⟩ stress of 4×10^8 dyn cm^{-2} we deduce from Fig. 15 an angular deviation of 10° from ⟨111⟩ towards ⟨110⟩. We assume the barrier width to be proportionally decreased from 35° to 25° and find from expression (6) with all other parameters unchanged: $|\eta'| = 1.15$ cm^{-1} or an increase by a factor of 2.1 as compared to the observed 2.8-fold increase (Fig. 16). This result may be considered very satisfactory; the larger experimental change may easily be due to a slight decrease in the barrier height under stress. It appears thus that the softness consists principally in a change of the *shape* of the defect-lattice interaction potential with the magnitudes of the anisotropies remaining essentially unchanged; this conclusion is consistent with those drawn in the discussion on the rigid aspects.

One might assume that the softness is an inherent property of systems with a large tunneling

splitting and hence a relatively weak hindered-rotation potential. There is, however, the KCl:Li^+ system, also a ⟨111⟩ -oriented tunneling defect, with a nn matrix element comparable to CN^- in KCl, $|\eta| \sim 0.55\ cm^{-1}$, in which no appreciable changes of the tunneling motion under uniaxial stress have been observed.[10,11]

VIII. COMPARISON TO HINDERED-ROTATION MODELS

As an alternative to the tunneling models Devonshire's model of hindered rotation[32] has been used to describe the CN^- systems.[4] Hindered-rotator models have the advantage to include higher librational states and are thus superior to tunneling models when librational states are so close to the ground state that the former cannot be neglected even in a first approximation. On the other hand the computation of hindered-rotator states and transitions is quite involved and an accurate fit of experimental data may require the study of a rather large variety of hindering potentials. Even though the present experimental results demonstrate the limited validity of any type of *rigid*-potential model for the description of CN^- in KCl an attempt has been made with the present data to find a best-fit hindering potential within the two-parameter manifold of potentials discussed in a recent work on hindered rotation.[33,34] The potentials considered there are given by

$$P(\phi, \theta) = K^4 V^4(\phi, \theta) + K^6 V^6(\phi, \theta)\ , \qquad (7)$$

where V^4 is the usual Devonshire potential and V^6 is the function of sixth order with cubic symmetry defined in Ref. 33. Three criteria were used to find best-fitting K^4, K^6 coefficients: (a) The minimum wells of the potential must be along ⟨111⟩ axes; (b) to account for the sharp double structure the four ground state levels have to be so nearly equidistant that the three transitions occurring between them differ in frequency less than ±10%; (c) the (average) splitting of the librational levels from the ground state ($11.5\ cm^{-1}$) has to be about 9.4 times the splittings between two adjacent ground-state levels ($1.25\ cm^{-1}$).

The values of K^4 and K^6 which meet the criteria are indicated in Fig. 21. Criterion (a) is met in the whole sector of the (K^4, K^6) plane shown in Fig. 21; (b) leaves a rather narrow segment (excluding $K^6 = 0$, i.e., the Devonshire model); the line of all potentials matching (c) cuts through this segment. No predetermined value was assigned to the rotational constant B in this fit. Comparison of experimental and model level schemes yields values for B very close to $1\ cm^{-1}$ for all points consistent with (a)–(c). For a typical point, $K^4 = -9.6$, $K^6 = -11.6$, experimental and computed vibration-rotation spectra are compared in Fig. 21. An arbitrary, constant linewidth was assigned in the computed spectrum to all transitions. But even neglecting differences in linewidths the experimental spectra differ quite significantly from the computed ones, especially in the structure of the librational sideband. This discrepancy is rather fundamental, because in order to obtain a narrower librational sideband, one would have to go to stronger potentials, but then the splitting of the librational sideband would be larger and criterion (b) could not be met. Even this best fit may thus not be considered satisfactory; either a rigid-hindered-rotator model is inherently unable to describe a soft tunneling system in detail even for zero stress, or the defect-lattice interaction po-

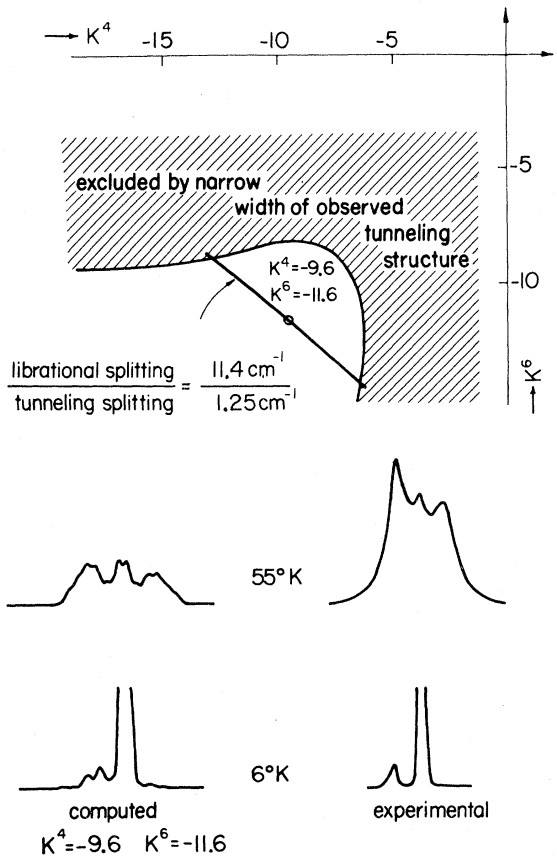

FIG. 21. Attempts to fit a hindered rotator potential to the experimental data. Top: points in the (K^4, K^6) plane matching the criteria: (a) minima of the potential are along ⟨111⟩ axes, (b) zero-field transitions are within 10% of the same frequency and (c) the ratio between the librational and the tunneling splittings correspond to the observed values of $11.4\ cm^{-1}/1.25\ cm^{-1}$; bottom: computed spectra for the point which matches the three criteria are compared to the experimental spectra for two temperatures.

tential is so peculiar that for its description higher-than-sixth-order cubic functions would be needed.

In the above discussion we have not explicitly considered any "dressing" effects, i.e., contributions of the surrounding lattice to the moment of inertia of the defect which were found to be very important in other reorienting defect systems.[35,36] Such effects may be responsible for the fact that the fitted value of B (~ 1 cm^{-1}) is slightly smaller than that of the "naked" CN^- molecule (1.25 cm^{-1}).

IX. COUPLING BETWEEN VIBRATIONAL AND TUNNELING MOTION

Throughout this analysis we have assumed that the tunneling level schemes for the two first vibrational states are identical. Almost all corresponding Stokes–anti-Stokes absorption lines are in fact, within experimental error, situated symmetrically on either side of the pure vibrational frequency. Only a few minor deviations were observed: For KCl the anti-Stokes line of the zero-field structure is broader than the Stokes line and there is even a clear indication of a double structure (e.g., see Fig. 18); and also under high ⟨111⟩ stress and $E_\perp$ (see Fig. 4) the absorption structure is not exactly symmetrical. The differences are, however, not large enough to motivate a more complex model with separate tunneling level schemes for the first two vibrational states.

X. CONCLUSIONS

High-resolution ir spectroscopy has yielded direct spectroscopic access to the tunneling states of a series of CN^- systems. By studying combined vibrational tunneling transitions the investigation of tunneling transitions could be displaced into the midinfrared, where continously tunable radiation is readily available.

The results demonstrate that tunneling states exist in alkali halides with surprisingly sharp and well-defined levels despite their inherent great susceptibility to internal strain and other crystal imperfections. For the first time transitions between different paraelastic states could be observed in conjunction with a vibrational transition so that the complete level scheme of a tunneling system could be deduced from the frequencies of observed absorption lines. This constitutes the most comprehensive experimental verification so far for the validity of level schemes derived from "tight-binding" tunneling models.

This novel, more detailed study of a tunneling system led naturally to the detection of some new features described here in terms of a phenomenological "soft" tunneling model in which the defect-lattice interaction potential is appreciably deformable by externally applied stress.

The results evidence common features and systematic trends as to the tunneling splittings, elastic dipole moments, and fractions of nontunneling CN^- molecules among the different CN^- systems studied. So far there is no comprehensive theory relating tunneling parameters and paraelastic splittings of reorienting defects to more fundamental atomic parameters. The present results hopefully stimulate efforts towards a theoretical understanding of the vast amount of experimental data available in that field.

ACKNOWLEDGMENTS

The author acknowledges the very fruitful cooperation with Professor F. Lüty during the course of this work and, in particular, for valuable assistance in the preparation of the manuscript. To Professor F. Rosenberger of the crystal growth laboratory the author is indebted for his great care taken in growing crystals of outstanding quality.

APPENDIX: SELECTION RULES AND TRANSITION MATRIX ELEMENTS FOR ELECTRIC DIPOLE TRANSITIONS BETWEEN TUNNELING STATES

Under the assumption of independent vibrational and rotational motion the selection rules and the relative strengths of the transitions discussed in this paper are exclusively determined by the rotational part of the transition matrix elements (we use in the following "rotational" and "tunneling" interchangeably to describe any property associated with the orientational coordinates ϕ and θ).

TABLE I. Selection rules for dipole transitions between states of O, D_2, D_3, and D_4 symmetry. Together with $g \leftrightarrow u$ they form the selection rules for transitions between the states of a ⟨111⟩ oriented tunneling defect on a cubic lattice site in the absence of external stress, and under ⟨110⟩, ⟨111⟩, or ⟨100⟩ stress, respectively.

O (no stress)	A_1	A_2	E	T_1	T_2
A_1				x	
A_2					x
E				x	x
T_1	x		x	x	x
T_2		x	x	x	x

D_4 (⟨100⟩ stress)	A_1	A_2	B_1	B_2	E
A_1		x			x
A_2	x				x
B_1				x	x
B_2			x		x
E	x	x	x	x	x

D_2 (⟨110⟩ stress)	A_1	B_1	B_2	B_3
A_1		x	x	x
B_1	x		x	x
B_2	x	x		x
B_3	x	x	x	

D_3 (⟨111⟩ stress)	A_1	A_2	E
A_1		x	x
A_2	x		x
E	x	x	x

Let ψ_i and ψ_f be two rotational eigenstates in a potential of symmetry G transforming as the irreducible representations R_i and R_f of G. With R_V we denote the (not necessarily irreducible) representation of G according to which transform the three components of a vector. An electric dipole transition from R_i to R_f is then only allowed if the direct product of the representations $R_i \times R_V \times R_f$ contains the trivial representation.

From this general principle the selection rules are easily derived for the symmetries of interest in this paper: O_h in the absence of external stress, D_{3d} under $\langle 111 \rangle$ stress, D_{2h} under $\langle 110 \rangle$ stress, and D_{4h} under $\langle 100 \rangle$ stress. As parity is a good quantum number in these symmetries the rule $g \longleftrightarrow u$ must always be obeyed. It remains then to consider the corresponding groups without inversion: O, D_3, D_2, and D_4 for which the selection rules are given in Table I.

The actual computation of tunneling transition matrix elements is illustrated with the following example. We use thereby the notation of Ref. 6 labeling the eight localized states of a $\langle 111 \rangle$ dipole by $\langle a| \cdots \langle h|$.

The wave functions of the A_{1g} and the B_{3U} tunneling states in the lower paraelastic multiplet under very high $\langle 110 \rangle$ stress (Fig. 1) are

$$\psi A_{1g} = \tfrac{1}{2}(\langle a| + \langle c| + \langle e| + \langle g|) ,$$
$$\psi B_{3U} = \tfrac{1}{2}(\langle a| + \langle c| - \langle e| - \langle g|) . \qquad (8)$$

Each localized state is assumed to have a unit dipole moment along the axis of its orientation. The transition matrix elements between the two states (8) for light polarized along the vertical z axis ($E_{\perp}^{\langle 001 \rangle}$) is then

$$\langle \psi A_{1g} | \cos\theta | \psi B_{3U} \rangle = \tfrac{1}{4}(\langle a| \cos\theta| a\rangle + \langle b| \cos\theta| b\rangle - \langle e| \cos\theta| e\rangle - \langle g| \cos\theta| g\rangle) = \tfrac{1}{3}\sqrt{3} .$$

†Supported by NSF Grant No. GH33704-XI. Helium provided by departmental grant from ONR.

*Supported by a Fellowship of the Swiss National Science Foundation. Present address: Brown Boveri, Research Center, CH-5401 Baden, Switzerland.

[1]V. Narayanamurti and R. O. Pohl, Rev. Mod. Phys. 42, 201 (1970).
[2]F. Lüty, Phys. Rev. B 10, 3677 (1974).
[3]A. D. Gongora and F. Lüty, Solid State Commun. 14, 923 (1974).
[4]W. D. Seward and V. Narayanamurti, Phys. Rev. 148, (1966).
[5]R. L. Pompi and V. Narayanamurti, Solid State Commun. 6, 645 (1968).
[6]M. Gomez, S. P. Bowen, and J. A. Krumhansl, Phys. Rev. 153, 1009 (1967).
[7]H. B. Shore, Phys. Rev. 151, 570 (1966).
[8]G. Pfister, Helv. Phys. Acta 39, 602 (1966).
[9]B. Dischler, Z. Naturforsch. A 25, 1844 (1970).
[10]D. Blumenstock, R. Osswald, and H. C. Wolf, Phys. Status Solidi 646, 217 (1971).
[11]T. R. Larson and R. H. Silsbee, Phys. Rev. B 5, 778 (1972).
[12]F. Bridges (unpublished).
[13]T. O. Eshelby, *Solid State Physics*, edited by F. Seitz and D. Turnbull (Academic, New York, 1956), Vol. III, p. 79.
[14]E. Kröner, *Ergebnisse der Angewandten Mathematik* (Springer, Berlin-Göttingen-Heidelberg, 1958), Vol. 5.
[15]A. S. Nowik and W. R. Heller, Adv. Phys. 14, 101 (1965).
[16]J. Muggli, Phys. Kondens. Mater. 12, 237 (1971).
[17]N. E. Byer and H. S. Sack, Phys. Status Solidi 30, 569 (1968).
[18]N. E. Byer and H. S. Sack, Phys. Status Solidi 30, 579 (1968).
[19]H. S. Sack and M. C. Moriarty, Solid State Commun. 3, 93 (1965).
[20]A. Lakatos and H. S. Sack, Solid State Commun. 4, 315 (1965).
[21]C. Y. Fong, Phys. Rev. 165, 462 (1968).
[22]R. A. Heredeen and R. H. Silsbee, Phys. Rev. 188, 645 (1969).
[23]R. W. Dreyfus, Solid State Commun. 7, 827 (1969).
[24]K. Knop and W. Känzig, Helv. Phys. Acta 46, 889 (1974).
[25]H. Burkard and W. Känzig, Helv. Phys. Acta 46, 729 (1973).
[26]H. U. Beyeler, R. Baumann, and W. Känzig, Phys. Kondens. Mater. 11, 286 (1970).
[27]W. E. Bron and R. W. Dreyfus, Phys. Rev. Lett. 16, 165 (1966).
[28]L. D. Schearer and T. L. Estle, Solid State Commun. 4, 639 (1966).
[29]G. Feher, I. W. Shepherd, and H. B. Shore, Phys. Rev. Lett. 16, 500 (1966).
[30]H. Härtel, Phys. Status Solidi 42, 369 (1970).
[31]L. D. Landau and E. M. Lifshitz, *Quantum Mechanics*, 2nd ed. (Pergamon, New York, 1965).
[32]A. F. Devonshire, Proc. R. Soc. A 153, 601 (1936).
[33]H. U. Beyeler, Phys. Status Solidi B 52, 419 (1972).
[34]H. U. Beyeler, J. Chem. Phys. 60, 4123 (1974).
[35]G. Pfister and W. Känzig, Phys. Kondens. Mater. 10, 231 (1969).
[36]S. Kapphan and F. Lüty, Phys. Rev. B 6, 1537 (1972).